IEEE Open Journal of
Intelligent Transportation
Systems

Received 30 January 2025; revised 29 May 2025; accepted 24 November 2025. Date of publication 26 November 2025; date of current version 4 December 2025.

Digital Object Identifier 10.1109/OJITS.2025.3637700

A Simulation-Based Efficient Optimization Method of an Odometry Localization Filter for Vehicles With Increased Maneuverability

CHENLEI HAN, MICHAEL FREY, AND FRANK GAUTERIN

Institute of Vehicle System Technology, Karlsruhe Institute of Technology, 76131 Karlsruhe, Germany

CORRESPONDING AUTHOR: C. HAN (e-mail: unljg@student.kit.edu)

This work was supported by the KIT Publication Fund of the Karlsruhe Institute of Technology.

ABSTRACT With the increasing level of driving automation, localization and navigation are not only used to provide positioning and route guidance information for users, but are also important inputs for vehicle control.Odometry localization method is the most widely used localization method due to its good short-term accuracy and cost-effectiveness, despite its known limitations like drift and environment dependency. Optimizing odometry remains a valuable area of research. By using the UKF-based odometry localization methode for vehicles with increased maneuverability introduced in our previous work, this paper presents a simulation-based optimization method to improve the accuracy of the odometry. This proposed simulation-based optimization method aims to achieve the accuracy goal with low computation effort. The covariance matrices of the UKF-based odometry are optimized by the particle swarm algorithm. In order to make the in simulation optimized covariance also applicable in the real vehicle, sensor error models are built up to generate realistic sensor signals. To reduce the computation effort during optimization an efficient driving maneuver, which covers more vehicle states is generated and used instead of normal parking maneuvers. The use of the efficient driving maneuver has been shown to reduce the optimization effort by approximately 60% without sacrifice the optimization effect. The efficacy of the optimized covariance matrices in enhancing odometry accuracy has been validated in both simulated and real-driving tests. The optimized odometry can reach an average end position error of 11cm and average end orientation error of 0.4°. Furthermore, a sensitivity analysis of sensor accuracy and noise level on odometry has been performed in the simulation environment with the help of the proposed optimization methods. Odometry using sensors of various accuracy and noise levels are optimized to achieve its best performance. The simulation results indicate the importance of the IMU sensor in the odometry localization method. This conclusion is supported by the results of a real driving test that used two IMU sensors with different accuracy and noise levels. The results of the sensitivity analysis provides a basis for sensor selection in vehicle system design.

INDEX TERMS Odometry, unscented Kalman filter, optimization, particle swarm optimization, omnidirectional, efficient manuever generation, sensor configuration.

ABBREVIATION

ABS	anti-lock braking system
AMR	anisotropic magnetoresistive sensor
ARW	angular random walk
ASR	anti slip regulation
BIS	bias instability
COG	center of gravity
CVG	Coriolis vibratory gyroscope
EKF	extended Kalman filter
ESP	electronic stability program
FGO	factor graph optimization
FOG	fibre optic gyroscope
GA	genetic algorithm
GNSS	global navigation satellite system
ICR	instantaneous center of rotation

The review of this article was arranged by Associate Editor Johannes Betz.

INS	inertial navigation system
IMM	interacting multiple model
IMU	inertial measurement unit
MEMS	micro-machined electromechanical system
PPR	pulse per revolution
PSO	particle swarm optimization
RLG	ring laser gyroscope
RMSE	root-mean-square error
RRW	rate random walk
UKF	unscented Kalman filter
YRS	yaw rate sensor.

NOMENCLATURE

Variables

$\bar{e_p}$	average position error
$\bar{e_{r,p}}$	relative position error
f	frequency
L	traveled distance
$\mathbf{Q}$	covariance matrix of system noises
$\mathbf{R}$	covariance matrix of measurement noises
r	vehicle turning radius
$S_{P_{95}}$	area enclosed by the 95th-quantile-line of position error.
v	vehicle Speed at COG
v_i	wheel velocity at i
$x\ y$	vehicle position in the global coordinate frames
β	vehicle side slip angle
δ_i	wheel steering angle at i
ε_i	wheel velocity angle at i
θ	vehicle orientation in the global coordinate frames
ω	vehicle yaw rate

Constant

$r_{i,x}$	distance between tire–road contact point and vehicle COG in vehicle longitudinal direction
$r_{i,y}$	distance between tire–road contact point and vehicle COG in vehicle lateral direction
Δt	sample time

Subscript

k	time step
i	position of wheel $i \in \{fl, fr, rl, rr\}$ stands for front left, front right, rear left and rear right

Superscript

$\times$	sensor measurements.

I. INTRODUCTION

With the increasing level of driving automation, localization and navigation will be used not only to provide users with positioning and routing information, but also to provide important inputs for safety-critical automated driving functions. This places high demands on the accuracy and robustness of localization. In addition to vehicle automation, the electrification of the automotive industry continues to advance. Since electric drives can be integrated into the wheel, the maneuverability of vehicles can be significantly improved (see Fig. 1) with the help of novel suspensions [1], [2]. The increased maneuverability presents new challenges for localization, especially for relative localization methods such as odometry.

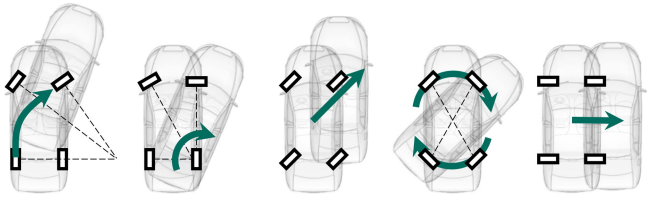

FIGURE 1. Possible driving modes using novel suspensions [3].

(a) (b) (c)

FIGURE 2. Demonstration vehicle with increased maneuverability, and its novel suspension at ±90° steering angle [3].

In a previous paper [3], a novel odometry localization method using an unscented Kalman filter (UKF) was developed for a demonstration vehicle [4]. This demonstration vehicle is equipped with a wheel individual steering system, which allows each wheel to achieve a 90° steering angle in both directions (Fig. 2). By using the extended vehicle models, the implemented novel odometry method is able to overcome the limitations of conventional odometry methods during omnidirectional parking maneuvers and obtains position errors less than 20 cm and orientation errors less than 1°.

However, the covariance matrices for the process noise $\mathbf{Q}$ and the observation noise $\mathbf{R}$ were determined in the previous paper empirically and therefore are not optimal. The full potential of the odometry has yet been realized. In addition, the results from the previous paper were based on high-quality sensors that are not realistic to be equipped in production cars. Therefore, it would be worthwhile to discuss which sensors play key roles in odometry application and how to reach a better odometry performance by using low-cost sensors. In this context, this paper proposes a simulation-based optimization method to achieve a more accurate odometry estimation. Based on the proposed optimization method, a sensitivity analysis of sensor accuracy and noise level on odometry will be performed in the simulation environment.

A. STATE OF THE ART

Localization methods for automated driving functions can be categorized into two types: global and relative localization.

The group of absolute localization methods includes first of all the global navigation satellite systems (GNSS). GNSS record the distances between the phase centers of the satellite and receiver antenna by measuring the time of

flight of the signal [5]. Real-time kinematic (RTK-GPS) can even provide a position with centimeter-level precision [6]. GNSS is characterized by long-term stable absolute accuracy. However, disturbances caused by environmental conditions that affect the measured variables of a GNSS receiver are problematic. They are caused by diffraction or reflection of electromagnetic waves on the earth's surface, mountains or buildings, and cause multipath reception [7] and thus errors in measurements. In landmark-based navigation, the object uses its own sensors to create a map of its environment and attempts to match it to a previously stored map to get the absolute position [8]. LiDAR and camera are two common sensors used to identify landmarks [9], [10], [11]. Landmark-based navigation provides higher localization accuracy in known environments. However, it is an expensive solution and depends on the environment.

The group of relative localization methods includes mainly inertial navigation system (INS) and wheel odometry.

An inertial navigation system uses an inertial measurement unit (IMU) to measure the three-dimensional values of vehicle acceleration and rotation speed. The acceleration and gyroscope measurements are integrated twice to determine the position and orientation of the vehicle. Typical for INS is the accumulation error, but the availability of an IMU is generally independent of external factors.

Wheel odometry (abbr. odometry) refers to a method for estimating the position and orientation of a mobile system based on the data of its propulsion system. In the automotive industry, measured variables from the chassis (wheel rotation), the yaw rate sensor and the steering (wheel steering angle or steering wheel angle) are generally used. Typical errors of odometry include error accumulation due to integration. Furthermore, there are environment-dependent errors due to high slip, for example due to a low coefficient of friction, high accelerations or driving through potholes. Incorrect model parameters of tires and chassis lead to considerable errors in position estimation. Nevertheless, odometry remains the most widely used localization method. It offers good short-term accuracy, is cost-effective and enables very high sampling rates. Odometry is always fused with other localization methods to increase the accuracy and ensure the robustness of the fused localization results [12]. Therefore, there is still a need to enhance the estimation results of odometry.

B. RELATED WORKS

The accuracy of state estimators can usually be increased by tuning filter parameters such as the covariance matrices $\mathbf{Q}$ and $\mathbf{R}$. The most common manual tuning method is the so-called divide-and-conquer strategy [13]. The first step is to obtain the covariance matrix for the measurement noises by statistically characterizing the difference between the sensor signals and the actual values [14]. Then the matrix for the process noises need to be determined. Since the process noises contain model and parameter uncertainties that cannot be easily quantified, it is often adjusted until the performance of the estimators is acceptable in the operational domain. This tuning method can satisfy most industrial requirements. Nevertheless, such tuning requires a deep understanding of the system and is a time-consuming and tedious procedure. Therefore, many studies have focused on searching the optimal covariance matrices.

One of the most mentioned terms is the adaptive Kalman filter in which the covariance matrices are estimated. It can be broadly classified into four categories [15]: covariance-matching [16], [17], [18], correlation techniques [19], [20], [21], maximum likelihood [22], [23] methods and Bayesian method [13], [24], [25]. The basic idea behind the covariance-matching method is to make the innovations or residuals consistent with their theoretical covariance. The innovation covariance is computed by subtracting the actual and predicted measurement and is used to compute $\mathbf{Q}$ and $\mathbf{R}$. This method can be used online, but cannot ensure positive definiteness of $\mathbf{Q}$ and $\mathbf{R}$ [23]. Regarding correlation techniques, a set of equations is derived relating the system matrices to the sample autocorrelation functions of innovations. These equations are solved simultaneously for $\mathbf{Q}$ and $\mathbf{R}$. The correlation methods are mainly applicable to time-invariant systems and estimate the covariance matrices in an offline setting [26]. Maximum likelihood or Bayesian methods formulate the covariance estimation problem as maximization of the likelihood function associated with the innovations [23].

Instead of estimating the covariance matrices, many works have tried to find the covariance matrices $\mathbf{Q}$ and $\mathbf{R}$ directly by implementing numerical optimization methods to find the minimum of a defined optimization criteria. The most popular algorithms are the two evolutionary algorithms: genetic algorithm (GA) [27], [28], [29], [30] and particle swarm optimization (PSO) [31], [32]. They are particularly suitable for the optimization problems with high dimensions and large search space, even if the structural knowledge about the problem is not available [33]. In some works, state-dependent optimization has been used to achieve higher estimation accuracy. In [34], various cluster analysis methods were performed to automatically classify parking maneuvers into different states and enable state-dependent optimization using Bayesian optimization in [35], an artificial neural network-based learning module was applied to learn the errors of a temperature sensor at different humidity levels, so that the measurement covariance $\mathbf{R}$ of the Kalman filter-based temperature estimator can be properly adjusted according to the actual humidity. Similarly, a fuzzy logic algorithm was used in [36] to adjust the covariance $\mathbf{R}$ according to the system state.

Recently, factor graph optimization-based (FGO-based) fusion provides a new way to optimize the state estimator. In this method, all measurements and states are encoded into a factor graph, and the sensor fusion problem is solved iteratively by using the Gauss-Newton algorithm [37]. This method also considers the historical measurements, which means that the delayed measurements can also be

handled. This method is commonly applied in GNSS/INS integration [38], [39], [40].

Another efficient way to improve the estimation result is to apply more accurate process and/or observation models. Reviewing the literature about odometry localization in robotics and automotive industry, the most widely used models are double-track kinematic model [41], [42], [43], linear single-track model [44] and kinematic yaw rate model [45], [46]. However, these models have their own limitations, such as imprecise wheel steering angles due to elasticity in the steering system, tire slip due to high longitudinal and lateral acceleration. In [14], a lookup-table model for the actual wheel steering angle was built using the trajectory measured by RTK-GPS to compensate this error during parking. In [47], vehicle lateral dynamic model was implemented to predict the side slip angle and thus improve the accuracy of the estimated position. A similar idea was presented in [48], in which an interacting multiple model (IMM) filter combined the extended Kalman filter (EKF) estimates from a kinematic vehicle model and a dynamic vehicle model to adapt to different driving conditions.

Properly parameterized models can significantly improve the accuracy of localization results. Tire dynamic radius, wheelbase and track width are the three most important parameters for odometry. Since these parameters are time-varying due to the suspension geometry and driving conditions, current research has mostly focused on parameter estimation. In [49] an EKF is applied to estimate the tire dynamic radius and the rear track from an onboard GNSS sensor. In [50] a laser sensor was used to measure the actual tire radius and a neural network was continuously trained based on localization information as ground truth. A calibration method with Gauss–Newton method and integrated Kalman filter using only cost-effective sensors was introduced in [47].

C. MAIN CONTRIBUTIONS AND OUTLINE

It is noticed that some papers [26], [54] mentioned the excessive computation time of offline optimization methods, in spite of the satisfactory optimization results. Besides the reason of the optimization algorithms themselves, not carefully designed maneuvers for optimization also lead to a huge data set because some maneuvers like starting and stopping are repeated. Without designing the maneuver properly, it will significantly waste computational resources. In this paper, a method to generate efficient maneuver for optimizing and validating the odometry is presented. This method make it possible to reduce the data volume, while all relevant driving states during parking are covered. The decoupling of the correlation between vehicle speed, yaw rate and side slip angle due to the novel suspension system is also considered in the maneuver generation.

Furthermore, compared to many other simulation-based optimization methods that only considered the unbiased Gaussian noise of sensor signals, more precise sensor models are applied in this paper. In combination with a validated multi-body vehicle dynamic model [53], more realistic sensor behavior can be achieved in the simulation, so that the optimized covariance matrices from the simulation can also be applied to real driving tests.

Furthermore, most research efforts on optimizing Kalman filter have focused on filter parameters, model quality and model parameters. Few studies have taken sensor configurations into account. Meanwhile, high quality sensors are usually used in research works such as [51], [52], which are not realistic to be equipped in production vehicles. In this paper, with the help of the proposed optimization method, a sensitivity analysis regarding sensor accuracy and noise is performed in the simulation environment. The result serves as a basis for the sensor selection during the system design.

The contributions of this paper can be summarized as follows:

- An efficient driving maneuver for the optimization is generated to reduce the computation time.
- Sensor models are built up to achieve realistic sensor signals, enabling the application of optimized covariance matrices from simulations in real driving tests.
- A sensitivity analysis regarding sensor accuracy and noise level on odometry is performed for the sensor selection for the system design.

In addition, combined with the modular concept for building state estimators from our previous contribution [3], [53], a systematic methodology for designing, optimizing and validating state estimators is proposed in this paper.

The structure of this paper is organized as follows: In Section II, the proposed methodology is presented at first. The odometry to be optimized from [3] and the optimization problem including algorithm and criteria are introduced in Section III. The sensor error models used for the sensitivity analysis are presented in Section IV. Section V gives details about the efficient maneuver generation method used for optimization and validation. Section VI briefly explains how optimization is done in the simulation environment. The optimization results from the simulation and real driving test are reported in Section VII. The conclusion and outlook are given in Section VIII.

II. PROPOSED METHODOLOGY

The proposed methodology for designing, optimizing and validating state estimators is illustrated in Fig. 3 using odometry as an example. The five columns in this figure are the relevant aspects of this methodology. The columns with green borders are the estimator relevant aspects. These are the estimator itself and the applied models and sensors. In addition, validation and data collection (blue bordered columns) are also considered in this methodology. The concrete steps in each aspect are represented by the rectangular boxes and labeled with lowercase letters in the upper left corner. A detailed description of these steps can be found either in the given paper or in the corresponding sections of this paper in the upper right corner.

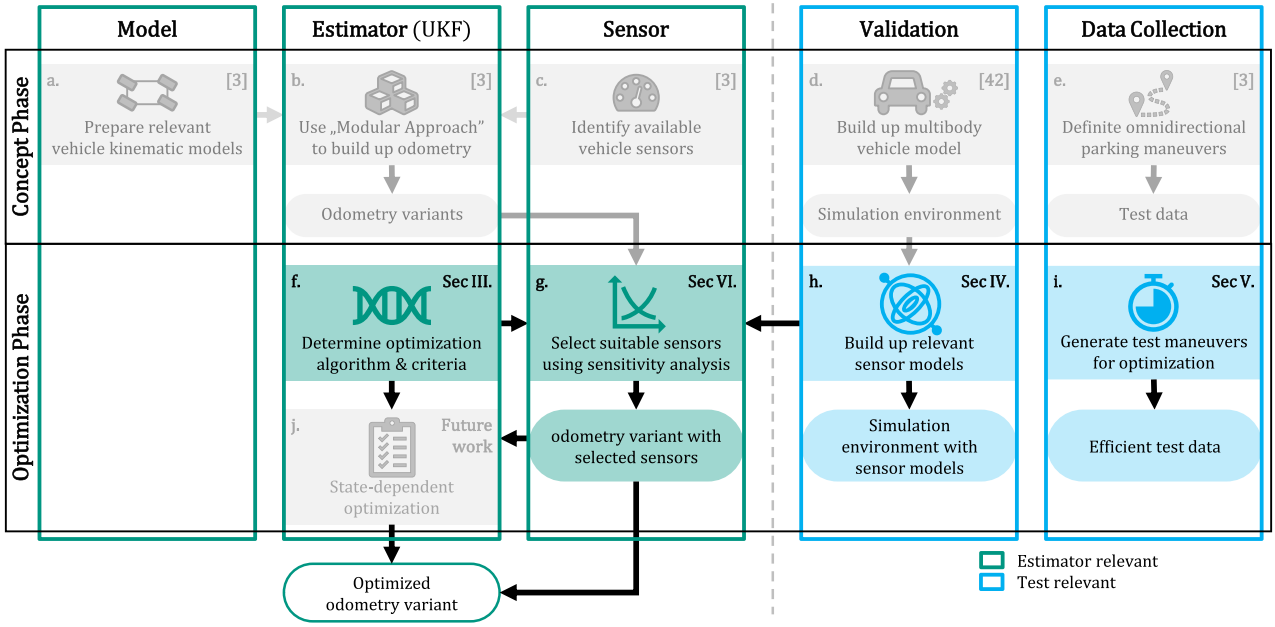

FIGURE 3. Proposed methodology of design, optimization and validation of state estimators. (Content of gray boxes are presented in [3], [53] and of color boxes in the corresponding sections in this paper. Box (j) is the planed work for the next step.)

The concept part is presented in grey, since they are already reported in [3], [53]. The main task of this part is to design odometry localization filters using the prepared vehicle kinematic models (a) and available sensors (c). A novel modular approach (b) was developed and applied to systematize this process. This approach enables the theoretical prediction of the accuracy of estimators without test data. To validate the odometry, a complex multi-body vehicle model (d) was built up and validated. Different omnidirectional parking maneuvers (e) have been defined.

The optimization part (presented in color) focuses on how to optimize the odometry, which is the aim of this paper. First, the optimization problem (f) is formulated by determining the tuning parameters, the optimization algorithm and criteria. To perform the sensitivity analysis for sensor selection, the established simulation environment in our previous work [53] is extended by sensor models (h). The proposed optimization method aims to improve not only the odometry accuracy, but also the optimization efficiency. Hence, test maneuvers for optimization are generated (i). In contrast to (e), target of (i) is to reduce the data volume and thus the optimization effort without sacrificing the quality of the optimization result. With the help of (f), (h) and (i), a sensitivity analysis can be performed, and the sensor configuration can be determined (g). State-dependent optimization (j) will be the next step of our research work.

III. OPTIMIZATION

A. SYSTEM DESCRIPTION

The odometry localization filter to be optimized originates from our previous publication [3]. 15 UKF-based odometry variants, differing in the applied system or observation models, were introduced and tested in terms of accuracy and robustness. The most accurate and robust variant will be optimized here. Its system states from time step k to $k+1$ are described as follows:

$$x_{k+1} = x_k + v_k \cdot \Delta t \cdot \cos\left(\beta_k + \theta_k + \omega_k \cdot \Delta t/2\right) \quad (1a)$$

$$y_{k+1} = y_k + v_k \cdot \Delta t \cdot \sin\left(\beta_k + \theta_k + \omega_k \cdot \Delta t/2\right) \quad (1b)$$

$$\theta_{k+1} = \theta_k + \omega_k \cdot \Delta t \quad (1c)$$

$$v_{k+1} = v_k \quad (1d)$$

$$\omega_{k+1} = \omega_k \quad (1e)$$

$$\beta_{k+1} = f_\beta\left(\varepsilon_{i,k}\right) \quad (1f)$$

$$\varepsilon_{i,k+1} = \arctan \frac{v_k \cdot \sin \beta_k + r_{i,x} \cdot \omega_k}{v_k \cdot \cos \beta_k - r_{i,y} \cdot \omega_k}. \quad (1g)$$

Eqs. (1a), (1b) and (1c) form the motion model, where $[x\ y\ \theta]^T$ are the vehicle position and orientation in the global coordinate frame. The vehicle velocity v and the yaw rate ω are predicted by (1d) and (1e) using the random walk model. β is the side slip angle and f_β in (1f) is a lookup-table model, which uses four wheel velocity angles ε_i to calculate β. Different from the wheel steering angle δ_i, the wheel velocity angle ε_i contains the tire slip angle α_i, that is $\varepsilon_i = \delta_i + \alpha_i$. Since α_i can only be measured with great effort, ε_i in (1g) is calculated by using v, ω and β. $r_{i,x}$ and $r_{i,y}$ are the distances between the center of gravity (COG) and the tire-road contract points in the vehicle longitudinal and lateral direction. The subscript i refers to the individual wheels $i \in \{fl, fr, rl, rr\}$. Δt stands for the sample time.

The UKF-based odometry uses the system model (1) to predict the states at first. These states are then updated

TABLE 1. Standard deviation of the covariance matrices in [3].

Variable	Value	Unit	Description
σ_x	$1 \cdot 10^{-6}$	m	position error
σ_y	$1 \cdot 10^{-6}$	m	position error
σ_θ	$1 \cdot 10^{-6}$	rad	orientation error
σ_v	$1 \cdot 10^{-2}$	m/s	velocity error
σ_ω	$1 \cdot 10^{-2}$	rad/s	yaw rate error
σ_β	$1 \cdot 10^{-2}$	rad	sideslip angle error
σ_{ε_i}	$1 \cdot 10^{-2}$	rad	wheel velocity angle error
$\sigma_{v_i^\times}$	$2 \cdot 10^{-1}$	m/s	wheel velocity noise
$\sigma_{\omega^\times}$	$8 \cdot 10^{-3}$	rad	yaw rate sensor noise
$\sigma_{\delta_i^\times}$	$4 \cdot 10^{-3}$	rad	wheel steering angle noise

through the observation models

$$v_{i,k}^\times = v_k \cdot \cos\left(\varepsilon_{i,k} - \beta_k\right) + \omega_k \cdot \left(r_{i,x} \cdot \sin\varepsilon_{i,k} - r_{i,y} \cdot \cos\varepsilon_{i,k}\right) \tag{2a}$$

$$\omega_k^\times = \omega_k \tag{2b}$$

$$\delta_k^\times = \varepsilon_k, \tag{2c}$$

by using the four wheel speed sensor signals $v_i^\times$, the yaw rate sensor signal $\omega^\times$ and the four wheel steering angle sensor signals $\delta_i^\times$.

B. FORMULATION OF OPTIMIZATION PROBLEM

1) CRITICAL PARAMETERS

According to the system description, the time-invariant covariance matrices $\mathbf{Q}$ and $\mathbf{R}$ are set to:

$$\mathbf{Q} = \mathrm{diag}\left(\sigma_x^2, \sigma_y^2, \sigma_\theta^2, \sigma_v^2, \sigma_\omega^2, \sigma_\beta^2, \sigma_{\varepsilon_i}^2\right) \tag{3a}$$

$$\mathbf{R} = \mathrm{diag}\left(\sigma_{v_i^\times}^2, \sigma_{\omega^\times}^2, \sigma_{\delta_i^\times}^2\right). \tag{3b}$$

They are determined empirically in [3]. These values are summarized in Table 1. As $[x, y, \theta]$ only depend on the state variables v, ω and β and themselves, the process noises of the motion model (1a), (1b) and (1c) were set to a very small value 10^{-6}, which means that the motion model was treated as a quite accurate model.

Theoretically it is possible to optimize all 10 parameters. For the reason that the motion model describes the general law of object motion and its output was decided by v, ω and β, we keep using the existing σ_x, σ_y and σ_θ for the motion model, so that the amount of the parameters to be optimized is reduced to seven.

2) OPTIMIZATION CRITERION

In most studies, the maximum or root-mean-square error (RMSE) of absolute position and heading error have been used as criteria of optimization. Such criterion are intuitive and easy to apply. But when multiple maneuvers are used for optimization, since each maneuver has a different distance and vehicle state, it is difficult to determine the weight of each maneuver. The optimized covariance matrices may only be the best for certain maneuvers.

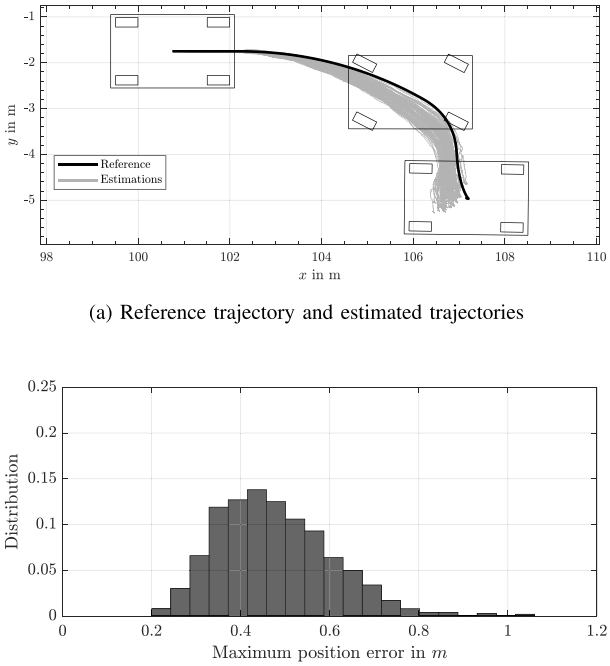

(a) Reference trajectory and estimated trajectories

(b) Probability distribution of the maximum position errors

FIGURE 4. Non-repeatability of Odometry Output.

Another factor to consider is the non-repeatability of the odometry output, which means that a given set of covariance matrices can produce different outputs for the same maneuver. As an example, Fig. 4 shows the distribution of the estimated trajectories (grey lines) and the histogram of the maximum position within 1000 simulations using the same covariance matrices. The root cause of this distribution can be explained as follows. Odometry is a relative localization method and the position and orientation of the vehicle are achieved by integrating the estimated v, ω and β with the help of the motion model (1a), (1b) and (1c). Since the quality of estimated v, ω and β depends on the sensor noise, it can also be said that the position and orientation are indirectly integrated by the sensor signals. Although the sensor noise is within a certain standard, it has its randomness. The errors due to the noise are sometimes compensated and sometimes accumulated leading to the unrepeatable odometry outputs. Therefore, it is not sufficient to evaluate the odometry for a certain maneuver only once.

Considering the two factors mentioned above, the optimization criterion used in this paper is described in Fig. 5. Suppose there are m parking maneuvers for the optimization process. For a particular parking maneuver, the position error can be plotted against the traveled distance (see Fig. 5(a)). After repeating the simulation for several times, the curves can form a banded area and we assume that the banded area will no longer extend after n repetitions.

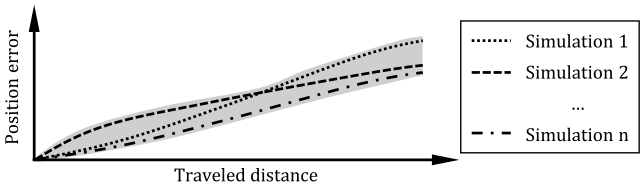

(a) Distribution of position errors in a certain maneuver

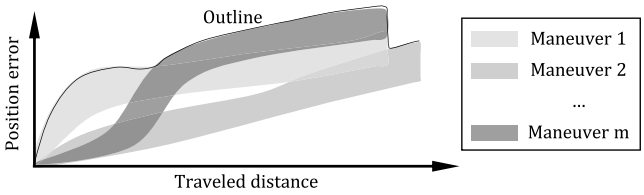

(b) Distribution of the position errors in all maneuvers

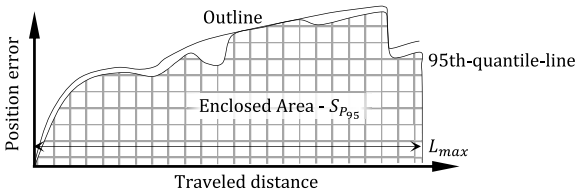

(c) 95-quantile of the position errors in all maneuvers

FIGURE 5. Optimization criterion.

After the banded areas of all m maneuvers are overlapped (see Fig. 5(b)), the contour of the overlapped area is able to contain the largest errors of all maneuvers over the traveled distance. By minimizing the enclosed area under the contour, the optimization result is not optimal but stable for each maneuver.

In practice, not the contour rather the 95th-quantile-line is applied (see Fig. 5(c)). The goal is to exclude the outlier, which will be optimized individually (process (j) in Fig. 3) in our future work. The 95th-quantile is determined empirically.

Furthermore, since odometry is a relative localization method, a criteria with the unit m/m is more intuitive and appropriate. So a relative position error is introduced here:

$$\bar{e_{r,p}} = \frac{S_{P_{95}}}{L_{max}^2} \tag{4}$$

where $S_{P_{95}}$ is the area enclosed by the 95th-quantile-line and L_{max} is the maximal traveled distance among the m test maneuvers.

3) OPTIMIZATION ALGORITHMS

Optimization algorithms begin with an initial variable and generate a sequence of improved estimates iteratively until optimization criteria are reached or boundary conditions are satisfied. The strategy used to move from one iterate to the next distinguishes one algorithm from another. Good algorithms should possess the properties of robustness, efficiency

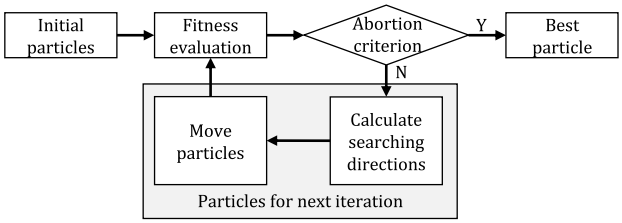

FIGURE 6. Flowchart of PSO.

and accuracy [55]. Since the optimization problem here is not differentiable, classic optimization methods such as gradient descent or quasi-Newton method are not suitable. In addition, there are seven parameters to optimize, which also leads to a large search space when using grid search or random search. Therefore, a metaheuristic method is considered here, which is able to deal with complex optimization problem with large search space. In this paper, Particle Swarm Optimization (PSO) [56] is applied, since PSO can converge faster than GA in our application according to our experience.

The PSO, which was first introduced by Kennedy and Eberhart [57], is a population-based stochastic search algorithm inspired by the social behavior of bird flocking. In PSO, the population is called a *Swarm* and each individual in the swarm is called a *Particle*. As shown in Fig. 6, the PSO begins by creating the initial particles, and assigning them initial velocities. It evaluates the fitness at each particle position, and determines the best location. The next searching directions of each particle are calculated based on the current velocity, the particles' individual best locations and the best locations of their neighbors. The particles move to the new positions and will be evaluated again. Iterations proceed until the algorithm reaches a stopping criterion.

IV. SENSOR MODELING AND CONFIGURATION

Different from demonstration vehicles, which can use high quality sensors for research purposes, the cost of each component in production vehicles requires careful consideration. It is also necessary to analyze how the sensor quality affects the estimation accuracy, which sensors dominate, so that an optimal sensor combination can be found. Such analysis are usually carried out in a simulation environment. The first step is to identify the sensor parameters and to build the sensor models.

A. WHEEL SPEED SENSOR

The speed signals are transmitted to ABS, ASR or ESP control unit of vehicle, which controls the braking force for each wheel individually. The navigation system also requires the wheel speed signals to calculate the traveled distance. The signals are generated by means of a steel signal plate to the wheel hub (for passive sensors) or multi-pole magnetic encoder (for active sensors) [58]. They have the same rotation speed as the wheel and move without contact along the sensitive area of the sensor head. Regardless of the sensor type, the output of speed sensors is usually rectangular pulse.

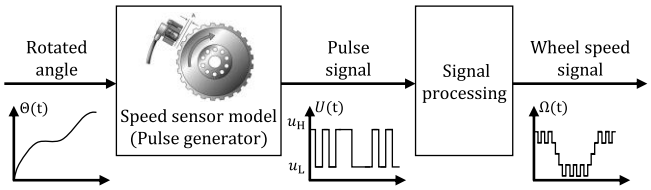

FIGURE 7. Model for wheel speed sensor and its signal processing.

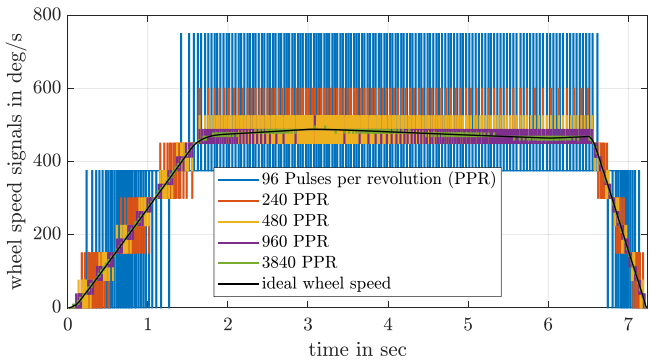

FIGURE 8. Wheel speed signals of different pulses per revolution (PPR).

We assume that all edges are detected. Then the pulse signals are only dependent on the true traveled angle and the number of pulses per revolution (PPR). The simulation of the wheel speed sensor signal is shown in Fig. 7. The pulse signal is generated using the ideal rotated angle of the wheel. The wheel speed is calculated by counting the number of pulses within the sample time Δt. Fig. 8 shows the wheel speed signals with 96, 240, 480, 960 and 3840 PPR. The higher the PPR, the lower the quantization error. The green curve with the highest PPR is the closest to the ideal wheel speed (black).

B. WHEEL STEERING ANGLE SENSOR

Modern steering angle sensors work with "anisotropic magnetoresistive sensors" (AMR), whose electrical resistance changes due to the orientation to an external magnetic field. Table 2 shows the specifications of steering angle sensors from different manufacturers for automotive applications. Accuracy and resolution are considered for the sensor modeling. The accuracy is modeled as white noise. For the simulation, we didn't take the data directly from the datasheets, but derived certain value classes from them. The data used are shown in Table 3.

C. YAW RATE SENSOR

Yaw rate sensor (YRS) is in principle gyroscope. There are mainly three types of gyroscope: ring laser gyroscope (RLG), fibre optic gyroscope (FOG) and Coriolis vibratory gyroscope (CVG). They tend to be large, expensive and used in aerospace and military applications. In contrast, MEMS (micro-machined electromechanical system) sensors, which use silicon micro-machining techniques, have fewer parts and are relatively inexpensive to manufacture [59]. According to the IEEE standard [60], the errors of a gyroscope are divided into deterministic and stochastic errors. The error model of a gyroscope is shown in Fig. 9. The deterministic errors include scaling error, axes misalignment, linear acceleration sensitivity and constant bias. The main components of the stochastic errors are *Angular Random Walk (ARW)*, *Bias Instability (BIS)* and *Rate Random Walk (RRW)*, which can also be referred to white, pink and brown noise, respectively. The differences are that the spectral density of white noise is constant with f, those of pink and brown are inversely proportional to $1/f$ and $1/f^2$ (where f is the frequency).

A full factorial parameter analysis for gyroscopes is too complex. Since the deterministic errors can usually be compensated by calibration, these types of errors are treated as constant in the simulation. Considering the RRW only has a long term effect on the signal and the duration of a parking process is usually less than a few minutes, the ARW and the BIS are identified as the main factors. In order to obtain reasonable parameters, several datasheets of the inertial measurement units (IMU) with application for automotive industry, including autonomous driving are collected. It can be seen in Fig. 10 that there is a certain relationship between ARW and BIS in logarithmic coordinate system. After fitting the curve, we selected eight points for the following simulations. The concrete parameter can be found in Table 4. The given resolutions are chosen so that the quantization errors do not dominate to the errors.

TABLE 2. Accuracy specification of available steering angle sensors.

Manufacture	Model	Range in °	Accuracy in °	Resolution in °
Danfoss	SASA	360	3.6	0.1
Bosch	LWS	780	2.5	0.1
Bourns	6002	780	2	0.1
Methode	SAS	1080	1.5	0.1
Kistler	CMSWA	1250	1.25	0.1
Hella	-	738	0.7	0.01
Kistler	5612A	1250	0.1	0.01

TABLE 3. Parameters of steering angle error models used in simulation.

Number	Accuracy in °	Resolution in °
1	5	0.1
2	2	0.1
3	1	0.1
4	0.5	0.01
5	0.1	0.01

V. EFFICIENT MANEUVER GENERATION METHOD

Driving maneuvers are required to perform the optimization. In our previous paper [3] we presented eight scenarios that can benefit from the increased maneuverability of the vehicle. A total of 35 parking maneuvers were derived from the eight scenarios and used for the validation. These

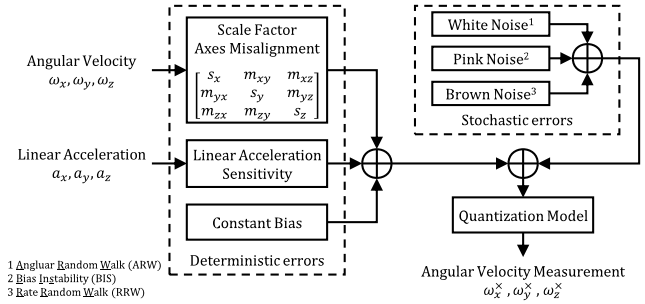

FIGURE 9. Error model of a gyroscope.

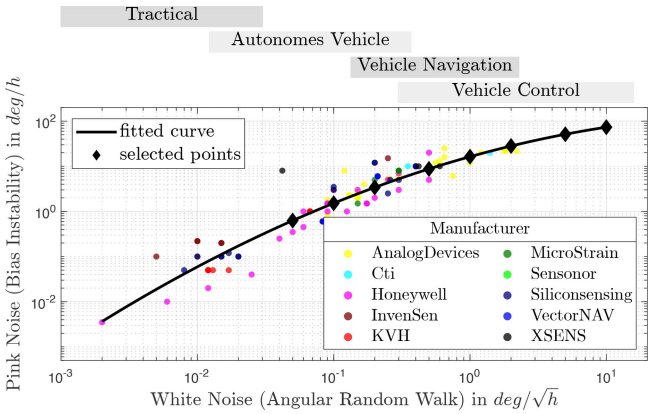

FIGURE 10. Features of gyroscopes for different applications.

TABLE 4. Parameters of gyroscope error models used in simulation.

Number	ARW in $^\circ/\sqrt{h}$	BIS in $^\circ/h$	Resolution in $^\circ$
1	10	65	0.1
2	5	50	0.1
3	2	25	0.05
4	1	17	0.01
5	0.5	10	0.01
6	0.2	3.6	$2 \cdot 10^{-7}$
7	0.1	1.5	$2 \cdot 10^{-7}$
8	0.05	0.5	$2 \cdot 10^{-7}$

maneuvers can also be used for the optimization in this paper. However, using the 35 maneuvers directly for the optimization is time consuming and not efficient as many vehicle states such as starting and stopping are repeated in each maneuver.

In order to reduce the amount of data during the optimization without sacrificing its quality, a method to generate efficient maneuver specifically for the demonstration vehicle is introduced. The goal is to generate a maneuver that covers as many of the relevant vehicle states for parking as possible.

According to the motion model (1a), (1b) and (1c), these three vehicle state variables v, ω and β need to be determined to generate the trajectory x, y and θ. For vehicles with front steering only, this is a two dimensional problem during the low speed parking maneuvers, because β is a function of v and ω [61]:

$$\beta = r_{i,y} \cdot \omega / v. \tag{5}$$

With the introduction of wheel individual steering system, this relationship no longer exists. For example, when the vehicle is driving in parallel (see the third and fifth driving modes in Fig. 1), the side slip angle β can vary from –90° to 90° depending on the wheel steering angle, while the yaw rate ω remains zero. Therefore, these three vehicle state variables v, ω and β have to be determined separately to cover as many driving states as possible during parking.

A. ANALYSIS OF SYSTEM LIMITATION

Although these three vehicle state variables have to be determined separately, they are still constrained by physical limitations. A general permutation of these three vehicle state variables is not reasonable. Therefore, the physical limits of v, ω and β during parking need to be found out to exclude physically inaccessible vehicle states. v is limited to 7 km/h and β to ±90°.

In order to determine the limitation of ω, the location of the instantaneous center of rotation (ICR) has to be determined. As shown in Fig. 11(a), the ICR can be located at any point in the plane due to the ±90° wheel steering angle. It can be divided into four areas numbered 1, 2, 3, 4L and 4R. Note that when the ICR moves from one area to another, the vehicle must have a stop. For example, if the ICR moves from P1 to P2, both left wheels have to continue to rotate over 90° anticlockwise, which is impossible with this novel suspension. Thus, the vehicle hast to stop and the left wheels have to turn clockwise. But a stop is not necessary between 4L and 4R, because the ICR moves to infinity and comes back. In this paper, only area 4 is considered.

The maximum yaw rate can be reached when the ICR is very close to the line connecting the front and rear wheels (see Fig. 11(b)). The value range of ω is then:

$$\omega \in \left[-\frac{|v|}{r_{min}}, \frac{|v|}{r_{min}} \right]. \tag{6}$$

In Fig. 12, the defined physical range of v, ω and β is shown as a grey boundary surface in a three-dimensional plot. Compared to the vehicle states from real driving tests (light blue crosses), there are still many vehicle states that are not reachable in reality. The reason for this is that the maximum lateral acceleration has not been taken into account. Considering the relationship $\omega = a_y/v$, ω has to be further limited. Based on the measurements from the real parking maneuvers from [3], the maximum of a_y is set to 0.5 m/s^2 for parking. The boundary surface in green therefore matches the measurement data better than before.

B. GENERATION OF TARGET MANEUVERS

As the boundaries of these three vehicle state variables are known, the stationary states are generated homogeneously

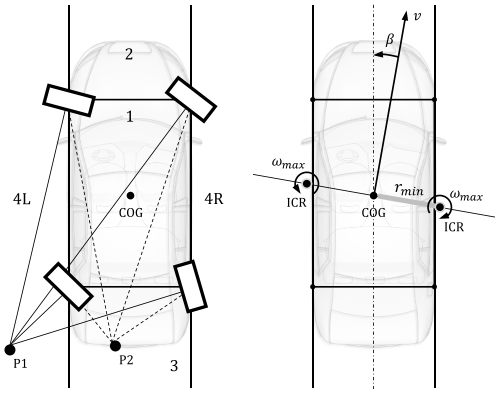

(a) Location of ICR (b) Max. yaw rate

FIGURE 11. System limitation of the demonstration vehicle.

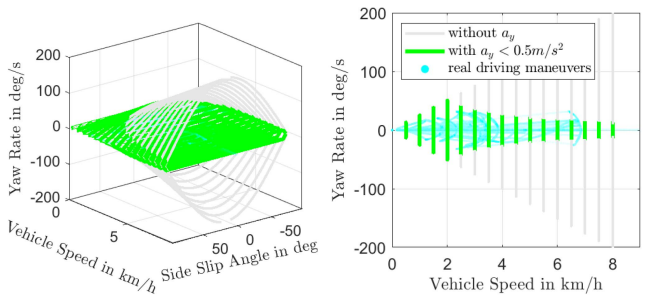

(a) 3D view (b) 2D projection

FIGURE 12. Determination of maximum lateral acceleration.

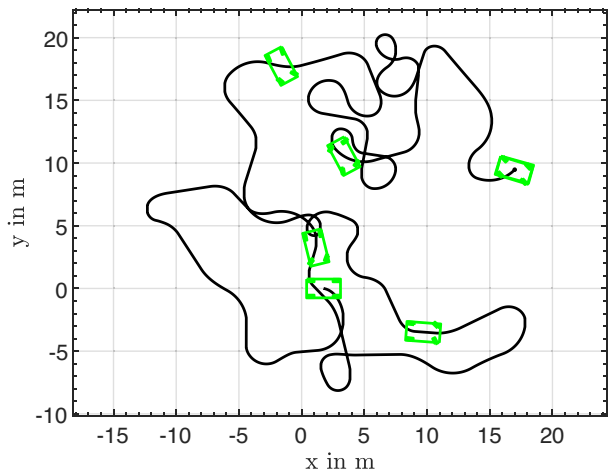

FIGURE 13. Generated efficient maneuver.

within the boundary surface. The vehicle starts from the zero state. The next state is always the closest one to the last one. Each state lasts for five seconds and the transition time is set to three seconds. The generated trajectory can be seen in Fig. 13. The generated maneuver is then divided into several segments with a distance of 25 meters to pass the distance of normal parking use cases.

For distinction, the efficient maneuver introduced in this paper is called DSE (Dataset Efficient") and the collective

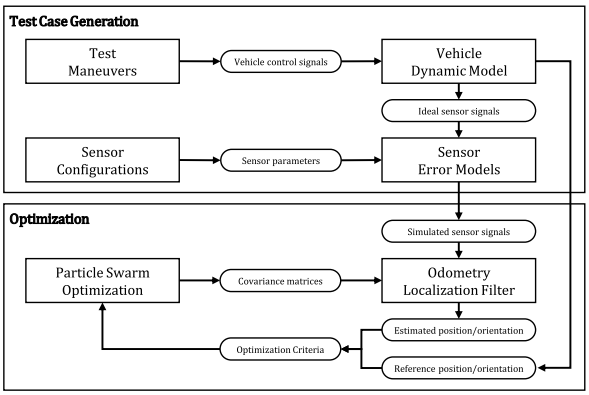

FIGURE 14. Implementation of optimization process.

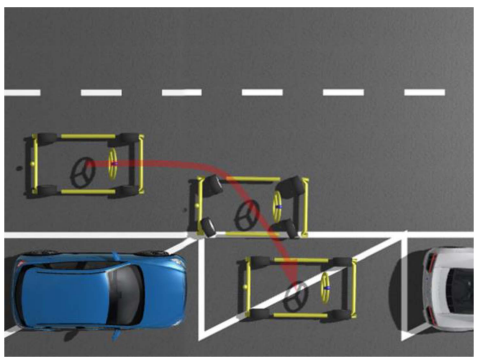

FIGURE 15. Visualization of omnidirectional parking maneuver in simulation environment.

of the maneuvers from our previous paper ist called DSA (Dataset All").

VI. SIMULATION-BASED OPTIMIZATION

Fig. 14 shows how the optimization is carried out in the simulation environment. It consists of two steps: test case generation and optimization.

In the first step, a validated multi-body dynamic model [53], including the novel suspension and steering system, is used to generate the ideal sensor signals and the reference position and orientation for the test maneuvers (see visualization in Fig. 15). Based on the ideal sensor signals, simulated sensor signals are generated according to the sensor configuration by using the sensor error models. In the second step, these simulated sensor signals serve as inputs to the odometry localization filter. The particle swarm optimization algorithm begins to find the optimal covariance matrices for the odometry based on the estimated and reference position and orientation.

The optimization is performed by using DSE and DSA separately.

VII. RESULTS

A. SIMULATION RESULTS

First we look at the result of two representative omni-directional parking maneuvers after optimization. Fig. 16

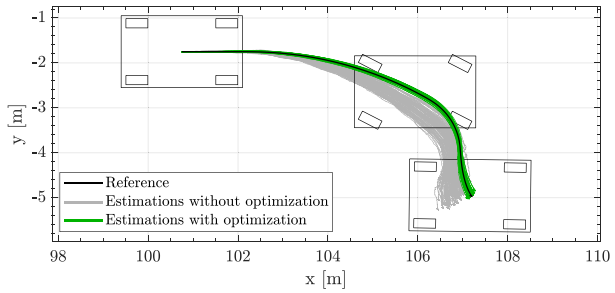

(a) Reference trajectory and estimated trajectories (side parking)

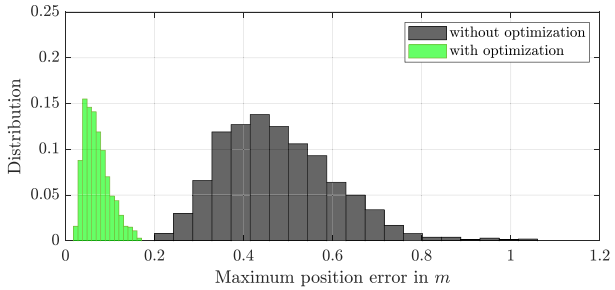

(b) Probability distribution of the maximum position errors (side parking)

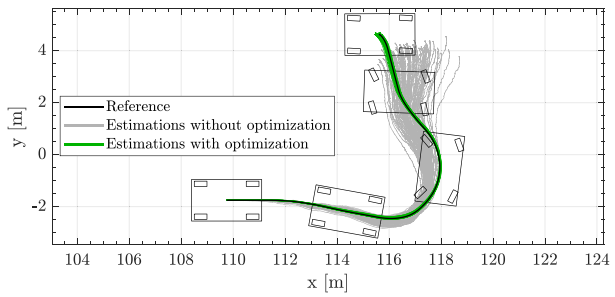

(c) Reference trajectory and estimated trajectories (parking on the opposite street)

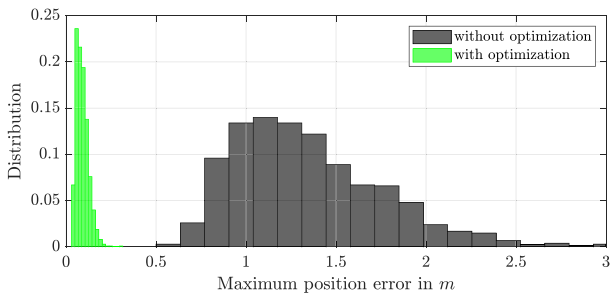

(d) Probability distribution of the maximum position errors (parking on the opposite street)

FIGURE 16. Optimization Result of Example Maneuver.

shows the estimated trajectories of these two parking maneuvers before and after optimization. It can be seen that not only the accuracy is improved, but also the distribution of the trajectory errors is narrower.

TABLE 5. Comparison of DSA and DSE.

	Total distance in m	Total duration in s
DSA	515	603
DSE	219	264

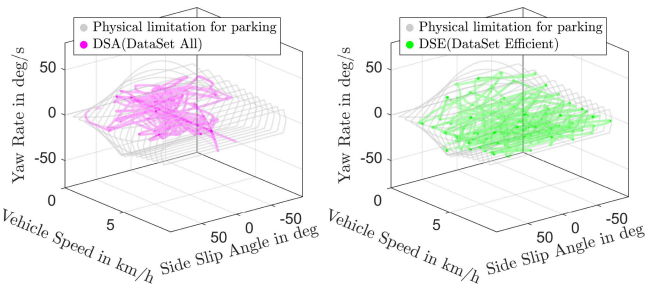

(a) DSA (b) DSE

FIGURE 17. Vehicle States from DSA and DSE.

1) EFFICIENT MANEUVER GENERATION

Before looking at the optimization results, a comparison between DSA and DSE is shown. Table 5 contains the sum of the distances of the maneuvers (total distance) and the time taken to complete the maneuvers (total duration). As the sample time of these two datasets is the same (10 ms), the data size of DSE is much smaller than that of DSA. The obvious advantage of DSE is that the time required for optimization can be significantly reduced. Fig. 17 also shows the plot of the covered vehicle states of DSE (green) and DSA (pink). The physical limitation of the vehicle during parking is shown in grey. Many of the vehicle states of DSA are in the low speed, low yaw rate and low side slip angle range because there are many repeated situations such as staring and stopping. On the contrary, DSE has a high vehicle state coverage, since the vehicle states are specifically generated. With a high vehicle state coverage, more critical situations can be detected and considered in the optimization. The distribution of DSE in the 3D space is also more homogeneous than that of DSA, which also helps save time to optimize for same vehicle states.

The results are presented in Fig. 18 and 19. The odometry has been optimized by using these two datasets, respectively. Afterward, the optimized odometry has been validated again through these two datasets.

In Fig. 18, the validation was done by DSA. Fig. 18(a) shows the relative position errors and Fig. 18(b) the relative orientation errors in logarithmic coordinates. The x-axis is the number of steering angle sensors. The x-axis is classified according to the used yaw rate sensors (YRS). The wheel speed sensor can be distinguished by the type of marker. The higher the number, the better the sensor quality. It can be seen that the odometry optimized by DSE (green) can reach almost the same accuracy level as the odometry optimized

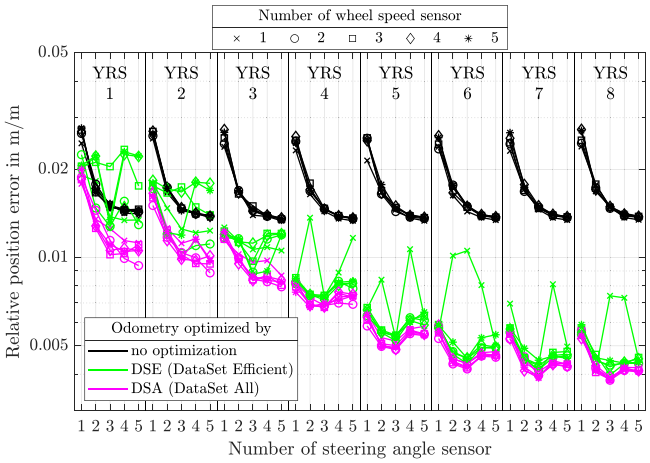

(a) Relative position error

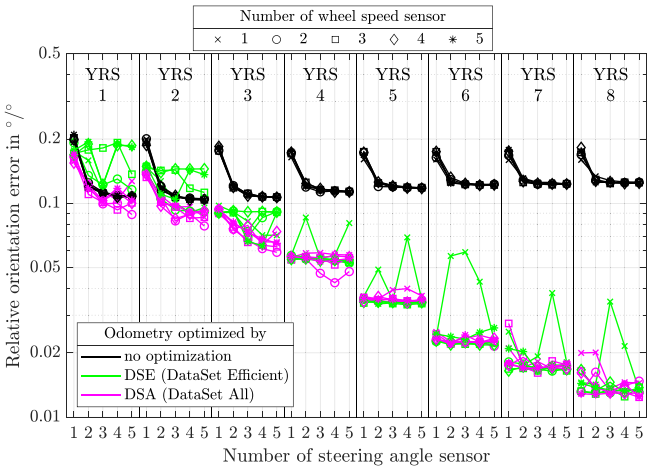

(b) Relative orientation error

FIGURE 18. Validation of the optimized odometry through DSA (DataSet All).

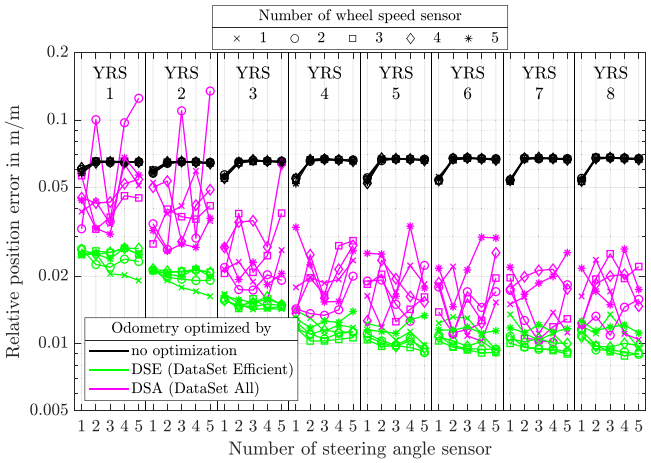

(a) Relative position error

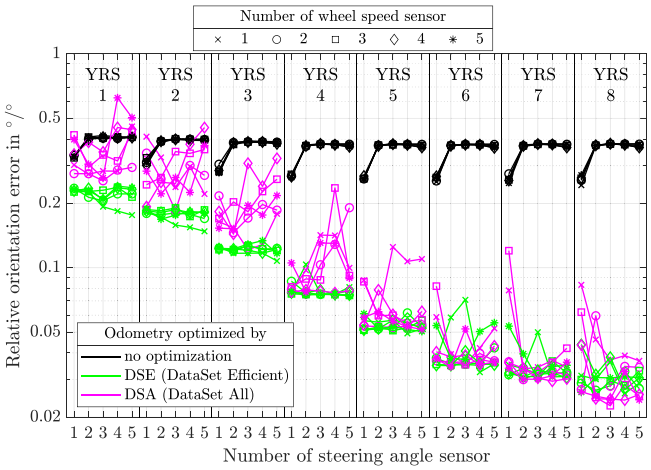

(b) Relative orientation error

FIGURE 19. Validation of the optimized odometry through DSE (DataSet Efficient).

by DSA (pink) if the wheel speed sensors are better than no.1 and the yaw rate sensors better than no.3.

In Fig. 19, the odometry has been validated by DSE. The advantage of the odometry optimized by DSE is obvious. The odometry optimized by DSA cannot achieve the same accuracy in almost all cases.

Why the DSE optimized odometry has a better performance can be explained by the vehicle state coverage of DSE and DSA. Since the vehicle states of DSE cover almost all of the vehicle states of DSA, the covariance matrices optimized by DSE are able to face most of the states in DSA.

However, there are still outliers in the DSE optimized odometry. The possible reasons why the DSE optimized odometry with yaw rate sensors no.1 and 2 are even worse than the unoptimized odometry (in Fig. 19) can be: (1) The optimization potential of odometry by using low quality yaw rate sensors is small. It is difficult for PSO to find covariance matrices in a limited number of iterations and to face the high vehicle state coverage of DSE. It is possible to find stable covariance matrices after extremely increasing the maximum iterations, but the time effort and needed resources within the optimization should also be considered. (2) Some vehicle states in DSA are also not contained in DSE, especially during state transitions. In contrast to the realistic use cases in DSA, DSE focuses only on the stationary states. The transitions in DSE are smooth, since the next stationary state is always geometrically the closest state to the current state during the maneuver generation.

2) SENSITIVITY ANALYSIS

With the help of Fig. 18 and 19, the results of the sensitivity analysis of the sensor accuracy and noise can now be extracted:

- The yaw rate sensor plays an essential role in position and angular accuracy. Especially after the optimization, the potential of high-precision yaw rate sensors is fully exploited.
- The yaw rate sensors currently used in production vehicles for driving dynamics applications and

TABLE 6. Real sensor parameters.

Sensor	Parameters
Bosch LWS 5.6.3 steering wheel sensor	accuracy 2.5°
	resolutiong 0.1°
Bosch BNO055 IMU	ARW $1°/\sqrt{h}$
	BIS not specified
UM7 IMU	ARW $0.3°/\sqrt{h}$
	BIS not specified
Integrated speed sensor in E-Motor	PPR 3840

navigation can be used depending on the accuracy requirements.
- An optimization to improve the odometry accuracy may not be necessary if low quality yaw rate sensor already meet the accuracy requirements of the applications.
- The PPR of the speed sensor does not plays a role after optimization.

B. REAL DRIVING TEST

1) PREPARATION

In this section, the covariance matrices optimized in the simulation environment are used in the real driving tests to check if the performance of the odometry is improved as in the simulation. The DSA maneuvers have been carried out. Due to the limited test area and safety reason, DSE could not be carried out. The parameters of the sensors used are listed in Table 6. In addition, two IMUs with different accuracy and noise levels were selected to plausibly demonstrate the dominant role of the IMU sensor in odometry.

The real driving tests have been executed in a hall with a flat surface. A ground truth system with RTK-GPS is not feasible in this environment without open air. To obtain the actual position and orientation of the vehicle, two laser pointers were attached to the frame, one at the center of the front plate and one at the center of the rear plate. Before the start and at the end of each test, the laser points were used to mark points on the ground. One way to measure the marked points is to create a coordinate system on the floor after the experiments. When setting up a coordinate system, it is essential that the X-Y axes are perpendicular to each other. In practice, however, it is challenging to ensure an exact right angle. To ensure precise measurement of the points marked on the floor, a method shown in Fig. 20 was used. The principle of this method is to measure the distance between two points instead of measuring the distance between a point and a line (X or Y axis) to avoid angular error. Before starting the measurement, two reference points (Ref 1 and Ref 2) have to be defined. The blue points (P_F and P_R) are the two points marked on the ground, whose positions need to be determined. The distances from each blue point to the two reference points (d_{F1}, d_{F2}, d_{R1} and d_{R2}) were measured

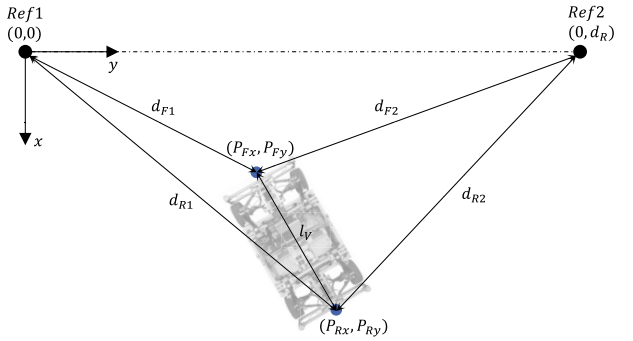

FIGURE 20. Method to measure the reference position of the vehicle.

with a laser distance measurer. The coordinates of P_F and P_R can be obtained by solving the following equations:

$$(P_{Fx} - 0)^2 + (P_{Fy} - 0)^2 = d_{F1}^2 \tag{7a}$$
$$(P_{Fx} - 0)^2 + (P_{Fy} - d_R)^2 = d_{F2}^2 \tag{7b}$$
$$(P_{Rx} - 0)^2 + (P_{Ry} - 0)^2 = d_{R1}^2 \tag{7c}$$
$$(P_{Rx} - 0)^2 + (P_{Ry} - d_R)^2 = d_{R2}^2 \tag{7d}$$

Please note that all blue points must be on one side of the connecting line between the two reference points to ensure the unique solution.

2) RESULTS OF UM7 IMU SENSOR

Fig. 21(a) shows one of the typical parking case, in which the vehicle parks parallel in the parking lot without turning and stopping. Fig. 21(b) shows estimated trajectories and the position and orientation error of odometry with the UM7 IMU. The four colors represent the results of no optimization, manual optimization, DSA-optimization and DSE-optimization respectively. The improvement achieved through the optimization is proofed.

The evaluation results of all test cases are shown in the left two plots in Fig. 22. The errors have been significantly reduced, especially the orientation error. Similar to the simulation result in Fig. 18 YRS 4, the DSA-optimized and DSE-optimized odometry have no significant different while using DSA to validate.

3) RESULTS OF BOSCH BNO055 IMU SENSOR

In addition to the results with UM7 IMU Sensor, the two right plots in Fig. 22 show the results with Bosch BNO055 IMU sensor. There is a slight improvement in the position estimation, while the orientation estimation has been obviously improved. The Bosch BNO055 IMU sensor has a comparable level of accuracy to the IMU model No.3 in Table 4. Compare to the simulation result in Fig. 18 YRS 3, the position estimation improvement aligns with the result from the simulation, while the orientation improvement in the real driving test shows slightly more enhancement compared to the simulation.

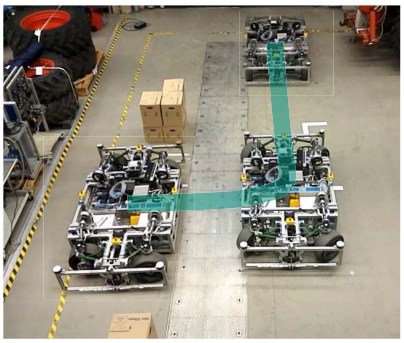

(a) real driving test

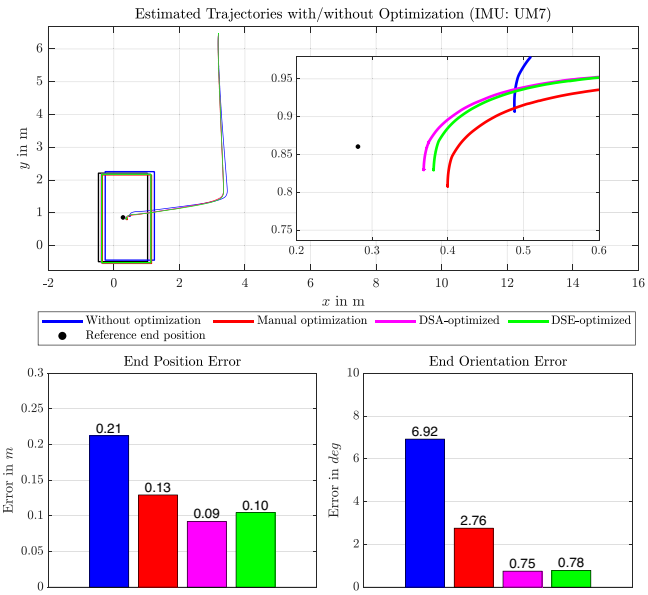

(b) Position and Orientation error with um7 IMU

FIGURE 21. Results of parallel parking without stopping.

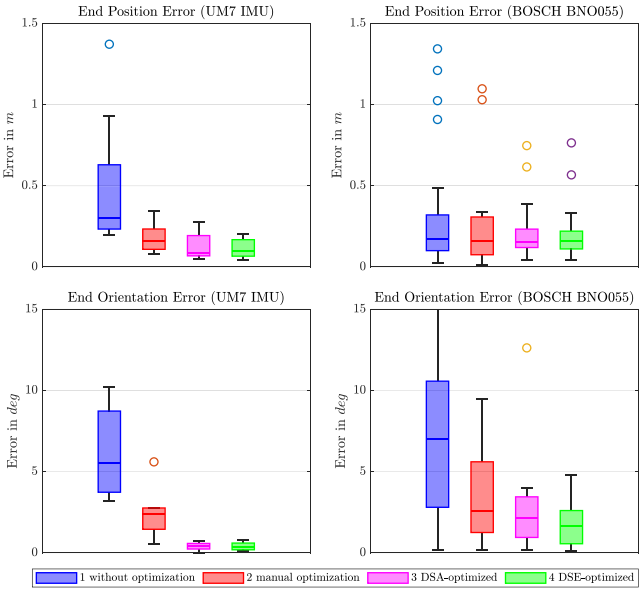

FIGURE 22. Boxplot of end position and end orientation errors with UM7 IMU.

4) COMPARISON UM7 vs BNO055 IMU

A comparison of the results with these two IMUs reveals that the UM7 IMU provides more accurate position and orientation estimates. This finding aligns with the simulation result, which demonstrates the pivotal role of the IMU in odometry.

C. LIMITATIONS

Not only the simulation, but also the real driving tests confirmed generally that the proposed simulation-based optimization method by using efficient driving maneuver can improved the odometry position and orientation estimation in the real driving tests. Nonetheless, some limitations need to be mentioned:

- Despite the modeling of sensor models aimed at achieving more realistic behavior, there remain discrepancies between these models and actual signals. The elasticity in the steering system might be quite large, which increases the error of the measured angle. The yaw rate sensor signal can be influenced by the vibration from the combustion engine or other mechanical vibrations in vehicles. The optimized covariance matrices might not be the optimal solution.
- Since the optimization criterion aims to have a stable result instead of optimal result, not all the test cases can be optimized. The optimized result in some cases is even worse than the original one, especially when the sensor accuracy is not high.
- The real driving tests were carried out in a hall with flat surface. The road conditions are very complex. Banked street, pothole can affect the optimization result.

VIII. CONCLUSION AND FUTURE WORKS

This paper presents a simulation-based optimization method for an odometry localization filter during omnidirectional parking maneuvers. The covariance matrices of the UKF-based odometry are optimized by the PSO algorithm. Sensor models are built up to generate realistic sensor signals, so that the optimized covariance from the simulation can also be applied in the reality. To reduce the optimization effort while ensuring a stable and accurate odometry result, a method for generating efficient driving maneuver was introduced. With the help of this method, the generated maneuver has a large vehicle state coverage, while the distance and duration of it are more than halved. The results from simulation and real driving tests show that using the generated efficient maneuver can still keep good optimization results. Based on the proposed method, a sensitivity analysis of sensor accuracy and noise on odometry was performed. The result shows an important role of IMU sensor in the position and orientation estimation.

In future work, the presented method for generating efficient maneuvers will be improved in terms of vehicle

state coverage and state transition. In order to carry out these maneuvers in real driving tests, the limited area of the test site must also be considered. Since the optimization criterion in this paper used the 95th-quantile of the outline of position errors, the vehicle states of the remaining 5% of the data need to be identified. A state dependent optimization for this 5% data will be carried out to improve the odometry accuracy of all vehicle states.

ACKNOWLEDGMENT

We would like to thank the Schaeffler Technologies AG & Co., KG for the provision of vehicle data and support in conducting test drives. Furthermore, we appreciate the valuable comments and suggestions of the anonymous reviewers for the improvement of this paper.

REFERENCES

[1] T. Bünte, L. M. Ho, C. Satzger, and J. Brembeck, "Zentrale fahrdynamikregelung der robotischen forschungsplattform robomobil," *ATZelektronik*, vol. 9, no. 3, pp. 72–79, 2014.

[2] M. Klein, A. Mihailescu, L. Hesse, and L. Eckstein, "Einzelradlenkung des forschungsfahrzeugs speed E," *ATZ-Automobiltechnische Zeitschrift*, vol. 115, no. 10, pp. 782–787, 2013.

[3] C. Han, M. Frey, and F. Gauterin, "Modular approach for odometry localization method for vehicles with increased maneuverability," *Sensors*, vol. 21, no. 1, p. 79, 2020.

[4] D. Nees, J. Altherr, M. P. Mayer, M. Frey, S. Buchwald, and P. Kautzmann, "Omnisteer—Multidirectional chassis system based on wheel-individual steering," in *Proc. 10th Int. Munich Chassis Symp.*, 2020, pp. 531–547.

[5] H. Winner, S. Hakuli, F. Lotz, and C. Singer, Eds., *Handbuch Fahrerassistenzsysteme* (ATZ/MTZ-Fachbuch), 3rd ed. Wiesbaden, Germany: Springer Vieweg, 2015.

[6] B. M. Scherzinger, "Precise robust positioning with inertially aided RTK," *Navigation*, vol. 53, no. 2, pp. 73–83, 2006. [Online]. Available: https://onlinelibrary.wiley.com/doi/abs/10.1002/j.2161-4296.2006.tb00374.x

[7] R. Vivacqua, R. Vassallo, and F. Martins, "A low cost sensors approach for accurate vehicle localization and autonomous driving application," *Sensors*, vol. 17, no. 10, p. 2359, 2017.

[8] B. Schlager, T. Goelles, M. Behmer, S. Muckenhuber, J. Payer, and D. Watzenig, "Automotive lidar and vibration: Resonance, inertial measurement unit, and effects on the point cloud," *IEEE Open J. Intell. Transp. Syst.*, vol. 3, pp. 426–434, 2022.

[9] A. Poulose, M. Baek, and D. S. Han, "Point cloud map generation and localization for autonomous vehicles using 3D Lidar scans," in *Proc. 27th Asia–Pacific Conf. Commun. (APCC)*, 2022, pp. 336–341.

[10] M. Yu, K. Gong, W. Zhao, and R. Liu, "Lidar and IMU tightly coupled localization system based on ground constraint in flat scenario," *IEEE Open J. Intell. Transp. Syst.*, vol. 5, pp. 296–306, 2024.

[11] P. K. Rai, N. Strokina, and R. Ghabcheloo, "Representation learning for place recognition using MIMO radar," *IEEE Open J. Intell. Transp. Syst.*, vol. 6, pp. 144–154, 2025.

[12] S. Harbers, J. Kalkkuhl, and T. van der Sande, "Vehicle egomotion estimation through IMU-radar tight-coupling," *IEEE Open J. Intell. Transp. Syst.*, vol. 6, pp. 244–255, 2025.

[13] Z. Chen, N. Ahmed, S. Julier, and C. Heckman, "Kalman filter tuning with Bayesian optimization," 2019, *arXiv:1912.08601*.

[14] A. Brunker, T. Wohlgemuth, M. Frey, and F. Gauterin, "Odometry 2.0: A slip-adaptive EIF-based four-wheel-odometry model for parking," *IEEE Trans. Intell. Veh.*, vol. 4, no. 1, pp. 114–126, Mar. 2019.

[15] R. Mehra, "Approaches to adaptive filtering," *IEEE Trans. Autom. Control*, vol. 17, no. 5, pp. 693–698, Oct. 1972.

[16] B. Jin, J. Guo, D. He, and W. Guo, "Adaptive Kalman filtering based on optimal autoregressive predictive model," *GPS Solut.*, vol. 21, no. 2, pp. 307–317, 2017.

[17] K. Myers and B. Tapley, "Adaptive sequential estimation with unknown noise statistics," *IEEE Trans. Autom. Control*, vol. 21, no. 4, pp. 520–523, Aug. 1976.

[18] S. Akhlaghi, N. Zhou, and Z. Huang, "Adaptive adjustment of noise covariance in Kalman filter for dynamic state estimation," in *Proc. IEEE Power Energy Soc. Gen. Meeting*, 2017, pp. 1–5.

[19] R. Mehra, "On the identification of variances and adaptive Kalman filtering," *IEEE Trans. Autom. Control*, vol. 15, no. 2, pp. 175–184, Apr. 1970.

[20] P. R. Belanger, "Estimation of noise covariance matrices for a linear time-varying stochastic process," *IFAC Proc. Vol.*, vol. 5, no. 1, pp. 265–271, 1972.

[21] B. J. Odelson, A. Lutz, and J. B. Rawlings, "The autocovariance least-squares method for estimating covariances: Application to model-based control of chemical reactors," *IEEE Trans. Control Syst. Technol.*, vol. 14, no. 3, pp. 532–540, May 2006.

[22] R. Kashyap, "Maximum likelihood identification of stochastic linear systems," *IEEE Trans. Autom. Control*, vol. 15, no. 1, pp. 25–34, Feb. 1970.

[23] V. A. Bavdekar, A. P. Deshpande, and S. C. Patwardhan, "Identification of process and measurement noise covariance for state and parameter estimation using extended Kalman filter," *J. Process Control*, vol. 21, no. 4, pp. 585–601, 2011.

[24] Z. Chen, C. Heckman, S. Julier, and N. Ahmed, "Weak in the NEES?: Auto-tuning Kalman filters with Bayesian optimization," 2018, *arXiv:1807.08855*.

[25] C. Hilborn and D. Lainiotis, "Optimal estimation in the presence of unknown parameters," *IEEE Trans. Syst. Sci. Cybern.*, vol. 5, no. 1, pp. 38–43, Jan. 1969.

[26] Y. Bulut, *Applied Kalman Filter Theory*. Boston, MA, USA: Northeastern Univ., 2011.

[27] Z. Du, Z. Cai, L. Chen, and H. Deng, "An evolutionary algorithm and Kalman filter hybrid approach for integrated navigation," in *Advances in Computation and Intelligence* (Lecture Notes in Computer Science 5821), Z. Cai, Z. Li, Z. Kang, and Y. Liu, Eds. Heidelberg, Germany: Springer, 2009, pp. 211–216.

[28] T. O. Ting, K. L. Man, E. G. Lim, and M. Leach, "Tuning of Kalman filter parameters via genetic algorithm for state-of-charge estimation in battery management system," *Sci. World J.*, vol. 2014, Aug. 2014, Art. no. 176052.

[29] L. Moreno, J. M. Armingol, S. Garrido, A. de La Escalera, and M. A. Salichs, "A genetic algorithm for mobile robot localization using ultrasonic sensors," *J. Intell. Robot. Syst.*, vol. 34, no. 2, pp. 135–154, 2002.

[30] J. Yan, D. Yuan, X. Xing, and Q. Jia, "Kalman filtering parameter optimization techniques based on genetic algorithm," in *Proc. IEEE Int. Conf. Autom. Logist.*, 2008, pp. 1717–1720.

[31] Y. Laamari, K. Chafaa, and B. Athamena, "Particle swarm optimization of an extended Kalman filter for speed and rotor flux estimation of an induction motor drive," *Elect. Eng.*, vol. 97, no. 2, pp. 129–138, 2015.

[32] N. Ramakoti, A. Vinay, and R. K. Jatoth, "Particle swarm optimization aided Kalman filter for object tracking," in *Proc. Int. Conf. Adv. Comput. Control Telecommun. Technol.*, 2009, pp. 531–533.

[33] S. Harbich, "Einführung genetischer algorithmen mit anwendungs-beispiel," 2007. [Online]. Available: http://wwwisg.cs.uni-magdeburg.de/sim/vilab/2007/papers/12_genetisch_sharbich.pdf

[34] A. Brunker, M. K. Paul, T. Wohlgemuth, M. Frey, and F. Gauterin, "Driving-condition dependent and Monte Carlo simulation-based optimization method for a Bayesian localization filter for parking," *IEEE Trans. Intell. Veh.*, vol. 5, no. 1, pp. 139–148, Mar. 2020.

[35] I. Ullah, M. Fayaz, and D. Kim, "Improving accuracy of the Kalman filter algorithm in dynamic conditions using ANN-based learning module," *Symmetry*, vol. 11, no. 1, p. 94, 2019.

[36] C. W. Kang and C. G. Park, "Attitude estimation with accelerometers and gyros using fuzzy tuned Kalman filter," in *Proc. Eur. Control Conf. (ECC)*, 2009, pp. 3713–3718.

[37] W. Wen, T. Pfeifer, X. Bai, and L.-T. Hsu, "Factor graph optimization for GNSS/INS integration: A comparison with the extended Kalman filter," *Navigation J. Inst. Navig.*, vol. 68, no. 2, pp. 315–331, 2021. [Online]. Available: https://navi.ion.org/content/68/2/315

[38] V. Indelman, S. Williams, M. Kaess, and F. Dellaert, "Factor graph based incremental smoothing in inertial navigation systems," in *Proc. 15th Int. Conf. Inf. Fusion*, 2012, pp. 2154–2161.

[39] W. Li, X. Cui, and M. Lu, "A robust graph optimization realization of tightly coupled GNSS/INS integrated navigation system for urban vehicles," *Tsinghua Sci. Technol.*, vol. 23, no. 6, pp. 724–732, 2018.

[40] W. Wen, X. Bai, Y. C. Kan, and L.-T. Hsu, "Tightly coupled GNSS/INS integration via factor graph and aided by fish-eye camera," *IEEE Trans. Veh. Technol.*, vol. 68, no. 11, pp. 10651–10662, Nov. 2019.
[41] T. D. Larsen, K. L. Hansen, N. A. Andersen, and O. Ravn, "Design of Kalman filters for mobile robots; evaluation of the kinematic and odometric approach," in *Proc. IEEE Int. Conf. Control Appl.*, 1999, pp. 1021–1026.
[42] M. Kochem, R. Neddenriep, R. Isermann, N. Wagner, and C.-D. Hamann, "Accurate local vehicle dead-reckoning for a parking assistance system," in *Proc. Amer. Control Conf.*, vol. 5, 2002, pp. 4297–4302.
[43] Y. K. Tham, H. Wang, and E. K. Teoh, "Adaptive state estimation for 4-wheel steerable industrial vehicles," in *Proc. 37th IEEE Conf. Decis. Control*, 1998, pp. 4509–4514.
[44] B. Gao, W. Tao, H. Chu, M. Tian, and H. Chen, "A reference vehicle model applied to electronic stability control (ESC) system," in *Proc. 36th Chin. Control Conf. (CCC)*, 2017, pp. 9436–9441.
[45] H. Chung, L. Ojeda, and J. Borenstein, "Accurate mobile robot dead-reckoning with a precision-calibrated fiber-optic gyroscope," *IEEE Trans. Robot. Autom.*, vol. 17, no. 1, pp. 80–84, Feb. 2001.
[46] V. R. Marco, J. Kalkkuhl, and T. Seel, "Nonlinear observer with observability-based parameter adaptation for vehicle motion estimation," *IFAC-PapersOnLine*, vol. 51, no. 15, pp. 60–65, 2018.
[47] M. Fazekas, P. Gáspár, and B. Németh, "Calibration and improvement of an odometry model with dynamic wheel and lateral dynamics integration," *Sensors*, vol. 21, no. 2, p. 337, 2021.
[48] K. Jo, K. Chu, K. Lee, and M. Sunwoo, "Integration of multiple vehicle models with an IMM filter for vehicle localization," in *Proc. IEEE Intell. Veh. Symp.*, 2010, pp. 746–751.
[49] A. Brunker, T. Wohlgemuth, M. Frey, and F. Gauterin, "GNSS-shortages-resistant and self-adaptive rear axle kinematic parameter estimator (SA-RAKPE)," in *Proc. IEEE Intell. Veh. Symp. (IV)*, 2017, pp. 456–461.
[50] J. Toledo, J. D. Piñeiro, R. Arnay, D. Acosta, and L. Acosta, "Improving odometric accuracy for an autonomous electric cart," *Sensors*, vol. 18, no. 1, p. 200, 2018.
[51] C. Cariou, R. Lenain, B. Thuilot, and M. Berducat, "Automatic guidance of a four-wheel-steering mobile robot for accurate field operations," *J. Field Robot.*, vol. 26, nos. 6–7, pp. 504–518, 2009.
[52] M. Brossard and S. Bonnabel, "Learning wheel odometry and IMU errors for localization," in *Proc. Int. Conf. Robot. Autom. (ICRA)*, 2019, pp. 291–297.
[53] M. Frey, C. Han, D. Rügamer, and D. Schneider, "Automatisiertes mehrdirektionales fahrwerksystem auf basis radselektiver radantriebe (OmniSteer): Schlussbericht zum Forschungsvorhaben," Institut für Fahrzeugsystemtechnik (FAST), Karlsruher Institut für Technologie (KIT), Karlsruhe, Germany, 2019.
[54] B. J. Odelson, M. R. Rajamani, and J. B. Rawlings, "A new autocovariance least-squares method for estimating noise covariances," *Automatica*, vol. 42, no. 2, pp. 303–308, 2006.
[55] J. Nocedal and S. Wright, *Numerical Optimization*. New York, NY, USA: Springer, 2006.
[56] R. Eberhart and J. Kennedy, "A new optimizer using particle swarm theory," in *Proc. 6th Int. Symp. Micro Mach. Human Sci.*, 1995, pp. 39–43.
[57] J. Kennedy and R. Eberhart, "Particle swarm optimization," in *Proc. Int. Conf. Neural Netw.*, vol. 4, 1995, pp. 1942–1948.
[58] K. Reif, *Sensoren Im Kraftfahrzeug*. New York, NY, USA: Springer-Verlag, 2012.
[59] O. J. Woodman, "An introduction to inertial navigation," Comput. Lab., Univ. Cambridge, Cambridge, U.K., Rep. UCAM-CL-TR-696, 2007.
[60] *IEEE Standard Specification Format Guide and Test Procedure for Coriolis Vibratory Gyros*, IEEE Standard 1431-2004, 2004.
[61] H.-J. Unrau, *Fahreigenschaften von Kraftfahrzeugen II*, Karlsruher Institut für Technologie (KIT), Karlsruhe, Germany, 2020.

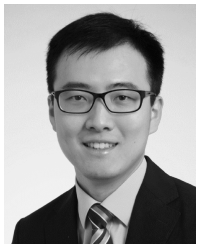

CHENLEI HAN received the B.Sc. degree in mechanical engineering from Tongji University in 2014, and the M.Sc. degree in mechanical engineering from the Karlsruhe Institute of Technology with focus on automotive engineering in 2017. Since 2017, he has been a Research Assistant with the Institute of Vehicle System Technology and started his Ph.D. regarding odometry localization. His current research interests include odometry, localization, state estimation, vehicle modeling, and virtual test.

MICHAEL FREY received the Diploma and Doctoral degrees in mechanical engineering from the University of Karlsruhe in 1993 and 2004, respectively. He is the Manager of the Research Group Automation and the Research Group Suspension and Propulsion Systems, Institute of Vehicle Systems Technology. His research interests are driver-assistance systems, operational strategies, suspension systems, vehicle dynamics, as well as vehicle modeling and optimization.

FRANK GAUTERIN received the Diploma degree in physics from the University of Münster, Germany, in 1989, and the Dr. rer. nat. degree (Ph.D.) in physics from the University of Oldenburg, Germany, in 1994. From 1989 to 2006, he was in various Research and Development positions with Continental AG, Germany, leaving as a Director of NVH Engineering, such as noise, vibration, and harshness. From 2006 to 2024, he was a Full Professor with the Karlsruhe Institute of Technology, Germany, a Head of the KIT Institute of Vehicle System Technology and scientific spokesperson of the KIT Mobility Systems Center. His research interests include vehicle control, vehicle dynamics, vehicle NVH, vehicle suspension, tire dynamics and tire-road-interaction, as well as vehicle concepts, vehicle modeling, and identification methods.